Received: 4 August 2023 | Revised: 18 December 2023 | Accepted: 21 December 2023

DOI: 10.1002/mrm.30008

Magnetic Resonance in Medicine

TECHNICAL NOTE

A silent echo-planar spectroscopic imaging readout with high spectral bandwidth MRSI using an ultrasonic gradient axis

Edwin Versteeg[1] | **Kyung Min Nam**[1] | **Dennis W. J. Klomp**[1] | **Alex A. Bhogal**[1] | **Jeroen C. W. Siero**[1,2] | **Jannie P. Wijnen**[1]

[1]Center for Image Sciences, Department of Radiology, University Medical Center Utrecht, Utrecht, The Netherlands

[2]Spinoza Centre for Neuroimaging, Amsterdam, Netherlands

Correspondence
Edwin Versteeg, Department of Radiology, University Medical Center Utrecht, Room Q.02.2.315 (HP E.01.132), Heidelberglaan 100 (PO Box 85500), 3584CX Utrecht, The Netherlands.
Email: e.versteeg-5@umcutrecht.nl

Funding information
HORIZON EUROPE Marie Sklodowska-Curie Actions, Grant/Award Number: 813120; Nederlandse Organisatie voor Wetenschappelijk Onderzoek, Grant/Award Number: 18361; Eurostars, Grant/Award Number: 11362

Abstract

Purpose: We present a novel silent echo-planar spectroscopic imaging (EPSI) readout, which uses an ultrasonic gradient insert to accelerate MRSI while producing a high spectral bandwidth (20 kHz) and a low sound level.

Methods: The ultrasonic gradient insert consisted of a single-axis (z-direction) plug-and-play gradient coil, powered by an audio amplifier, and produced 40 mT/m at 20 kHz. The silent EPSI readout was implemented in a phase-encoded MRSI acquisition. Here, the additional spatial encoding provided by this silent EPSI readout was used to reduce the number of phase-encoding steps. Spectroscopic acquisitions using phase-encoded MRSI, a conventional EPSI-readout, and the silent EPSI readout were performed on a phantom containing metabolites with resonance frequencies in the ppm range of brain metabolites (0–4 ppm). These acquisitions were used to determine sound levels, showcase the high spectral bandwidth of the silent EPSI readout, and determine the SNR efficiency and the scan efficiency.

Results: The silent EPSI readout featured a 19-dB lower sound level than a conventional EPSI readout while featuring a high spectral bandwidth of 20 kHz without spectral ghosting artifacts. Compared with phase-encoded MRSI, the silent EPSI readout provided a 4.5-fold reduction in scan time. In addition, the scan efficiency of the silent EPSI readout was higher (82.5% vs. 51.5%) than the conventional EPSI readout.

Conclusions: We have for the first time demonstrated a silent spectroscopic imaging readout with a high spectral bandwidth and low sound level. This sound reduction provided by the silent readout is expected to have applications in sound-sensitive patient groups, whereas the high spectral bandwidth could benefit ultrahigh-field MR systems.

KEYWORDS

EPSI, gradient insert, MRSI, quiet, silent, spectroscopy

1 | INTRODUCTION

MRSI enables the in vivo mapping of brain metabolites, whose alterations have been associated with various cancer types, multiple sclerosis, epilepsy, and other diseases that affect brain metabolism.[1,2] MRSI data quality benefits from higher magnetic field strengths through increases of the chemical shift dispersion and SNR.[3] This provides high-field MRSI with more sensitivity to distinguish low-SNR metabolite peaks and facilitates increased spatial resolution. However, the spectral encoding needed to acquire such data is intrinsically slow; for example, acquiring a single slice at high resolution (< 5 mm) might take about 30 min, limiting the clinical relevance of such MRSI acquisitions.[4,5] Therefore, several approaches exist that try to accelerate the MRSI acquisition, such as by shortening or removing suppression pulses and reducing the TR,[6,7] applying parallel-imaging methods,[8–10] or by using simultaneous spatial-spectral encoding (SSE).[11–15]

SSE accelerates MRSI by applying specific gradient waveforms during the FID, which increases the spatial encoding per TR. However, the time needed for this spatial encoding limits the spectral bandwidth of SSE methods when compared with phase-encoded MRSI and other acceleration approaches.[16] One of the earliest SSE methods is echo-planar spectroscopic imaging (EPSI), which features an EPI readout.[17,18] Here, the spectral bandwidth of an EPSI sequence is determined by the echo spacing of the EPI readout. Especially at high field (≥ 7 T) and high resolution, the acquisition of sufficient spectral bandwidth to capture all relevant metabolites using a single-shot EPSI is challenging, as it is limited by the maximum slew rate and available gradient strength. These parameters not only depend on the gradient hardware, but also on physiological limits of the subject, including the threshold for peripheral nerve stimulation and acoustic noise tolerance. Consequently, restrictions imposed on the EPSI readout by these parameters can limit the spatial resolution and spectral bandwidth.

The spectral bandwidth limitation can be mitigated by acquiring temporal interleaves in the form of multiple shifted or opposite-polarity EPI readouts.[19–23] However, this comes at the cost of scan time and a need to combine data from different EPSI readouts, which might lead to ghosting artifacts in the spectral domain. Alternatively, several non-Cartesian SSE techniques have been proposed that use rapidly oscillating gradient waveforms to encode k-space using either a spiral, concentric ring, or rosette k-space trajectory.[24–26] These methods can achieve a higher spectral bandwidth with a limited slew rate while featuring a high SNR efficiency. However, these high-resolution sequences coincide with severe acoustic noise levels at frequencies between 1 and 3 kHz, which is a sensitive range for the human hearing and may limit subject tolerance.[27,28]

To overcome some of the aforementioned challenges, we present a novel silent EPSI readout that allows for fast and high bandwidth spectroscopic imaging with low sound levels using an ultrasonic gradient axis. The ultrasonic gradient axis consists of a head gradient insert that produces a rapidly oscillating inaudible gradient waveform at 20+ kHz with an amplitude up to 40 mT/m and without inducing peripheral nerve stimulation.[29] Importantly, the additional spatial encoding provided by the ultrasonic gradient axis allows for the acquisition of fewer phase-encoding steps.[30] Additionally, the high oscillation frequency allows for an order of magnitude increase in spectral bandwidth (up to 20 kHz) compared with conventional SSE methods (1–3 kHz) without any ghosting artifacts. We will demonstrate the sound reduction through sound measurements and perform spectroscopic imaging experiments on a phantom to showcase the achievable acceleration, the extended spectral bandwidth, and measure the SNR efficiency and scan efficiency of our silent EPSI readout compared with phase-encoded MRSI and EPSI at 7 T.

2 | METHODS

2.1 | Ultrasonic gradient axis

An ultrasonic gradient axis was used to acquire the data, which was previously presented in Versteeg et al.[29] and featured a lightweight head gradient insert and an audio amplifier. The head gradient insert weighed 45 kg and was designed to be plug-and-play, which means it could be installed/removed within 15 min.[31] The audio amplifier was used to enable operation at 20 kHz and featured 18-kW peak power and 450-V peak voltage. A capacitor bank was used to make the gradient insert resonant at 20.34 kHz to compensate for the low peak voltage of the audio amplifier, which yielded a maximum amplitude of 40 mT/m at 20.34 kHz. The whole setup was controlled by an external waveform generator (Keysight) and was triggered by a TTL trigger for each TR.

2.2 | Silent EPSI readout

2.2.1 | Spatial encoding

The silent EPSI readout consists of an oscillating silent readout gradient that is played out during the acquisition

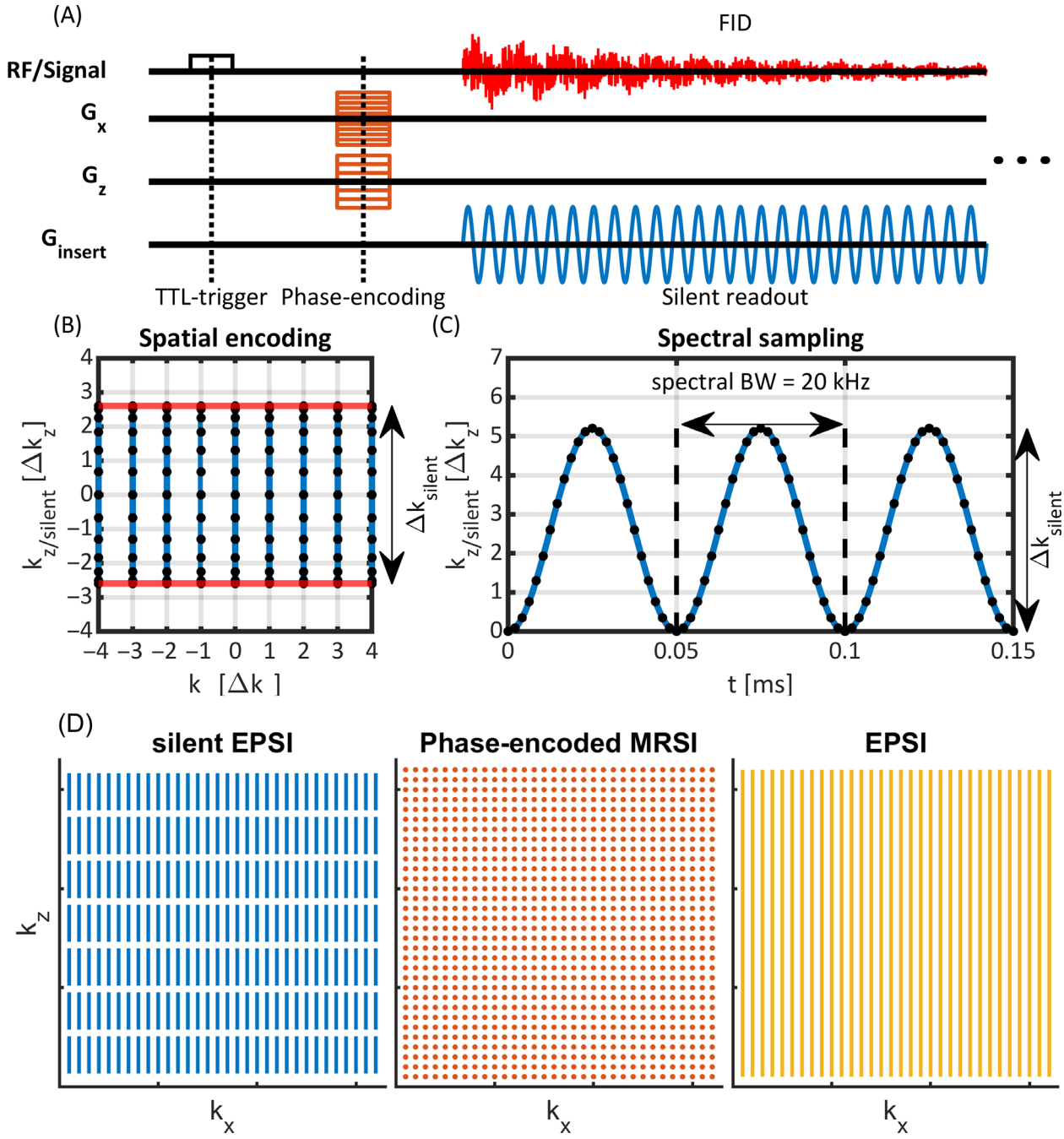

FIGURE 1 (A) Schematic depiction of the silent echo-planar spectroscopic imaging (EPSI) sequence (not to scale). Here, the silent EPSI readout operated in the z-direction, and the time between phase encode and readout was made longer for visualization purposes. (B) Schematic depiction of the spatial encoding provided by the silent EPSI readout. Here, the silent EPSI filled a line (in blue) in k-space each TR. (C) Schematic depiction of the spectral sampling from the silent EPSI readout. (D) Schematic depiction of the k-space filling using the silent EPSI compared with phase-encoded MRSI and conventional EPSI. Here, each TR is represented by a line in the silent EPI case, by a dot in the phase-encoded MRSI and by a longer line in the conventional EPSI readout.

of the FID or echo signal. Like other SSE methods, the spatial encoding provided by this additional gradient results in a larger k-space coverage per TR, which enables the acquisition of fewer phase-encoding steps. In Figure 1A, the silent EPSI readout is shown in the context of a phase-encoded MRSI experiment. The k-space trajectory generated by the silent readout gradient is given by the integral of the sinusoidal gradient waveform:

$$k_{\text{silent}}(t) = \frac{\frac{\gamma}{2\pi}G}{2\pi f}\cos(2\pi f t) \quad (1)$$

In Eq. (1), this k-space trajectory (k_{silent}) is shown to depend on the gyromagnetic ratio (γ in rad/s/T), the silent gradient amplitude (G in T/m), and the silent gradient oscillation frequency (f in Hz). For each TR, this k-space trajectory fills a line in k-space, as shown in Figure 1B. Here, the sample density along the line is determined by the number of samples acquired during each period of the k-space trajectory. Notably, the k-space coverage per TR (Δk_{silent}) of each line is determined by the peak-to-peak amplitude of this k-space trajectory, which is given as follows:

$$\Delta k_{\text{silent}} = \frac{\frac{\gamma}{2\pi} G}{\pi f} \tag{2}$$

Using Eq. (2), the reduction in phase-encoding steps for a fully sampled k-space can be obtained by comparing this k-space coverage of the silent readout with the phase-encoding steps of a phase-encoded MRSI acquisition, which can be written as

$$R_{\text{silent}} = \frac{\Delta k_{\text{silent}}}{\Delta k_{\text{phase-encode}}} = \Delta k_{\text{silent}} \text{FOV} \tag{3}$$

Equation (3) shows that the reduction in the number of phase-encoding steps (R_{silent}) linearly scales with the k-space coverage (i.e., the silent gradient amplitude and the FOV). This linear scaling with FOV only holds if the sampling in the silent gradient (k_z) direction is dense enough to meet the Nyquist criterion, which, in practice, is feasible for all FOV sizes relevant to the brain (e.g., up to 300 mm).

2.2.2 | Spectral encoding

Figure 1C shows the spectral sampling during the silent EPSI readout. Here, the maximum spectral bandwidth of the silent EPSI readout is theoretically limited to twice the oscillation frequency of the silent readout gradient (~40 kHz), which is the spacing between the positive and negative lobes of the readout. In practice, combining positive and negative gradient lobes can lead to ghosting artifacts like those that occur in conventional EPSI readouts. These ghosting artifacts can be avoided by limiting the spectral bandwidth of the silent EPSI readout to a maximum of 20 kHz.

2.3 | Spectroscopic imaging experiments

Spectroscopic imaging experiments were performed to compare the sound reduction, achievable acceleration, spectral bandwidth, and SNR/scan efficiency of the silent EPSI readout to phase-encoded MRSI and an EPSI readout without ramp-sampling. Here, we used a water-filled phantom (diameter = 10 cm) with 10 mL ethanol, 5 mL acetate, and 120 mg/m $CuSO_4$, that when considering water to resonate at 47 ppm (room temperature), have peaks at 3.2, 3.0, 1.9, and 0.95 ppm, which span a similar spectral bandwidth as ^{1}H brain metabolites. The gradient insert was positioned in a 7T (Achieva; Philips, Best, The Netherlands) MR scanner for all experiments. The gradient insert featured a birdcage RF coil, which was used for transmission. A 32-channel receive array (Nova Medical, Wilmington, MA, USA) was used for receiving ^{1}H signals.

All spectroscopic imaging data were acquired using a slice-selective FID acquisition with the following imaging parameters: a 192×192 mm^2 FOV, 6×6 mm^2 voxel size, 6-mm slice thickness, TE = 4.5 ms, TR = 1 s, 90° nominal flip angle (overtipped to compensate for low B_1 RF coil), VAPOR water suppression, and a spectral resolution = 4.45 Hz. The spectral bandwidth varied per acquisition technique and is specified below.

2.3.1 | Silent EPSI

During the silent EPSI readout, the ultrasonic gradient was operated at 40 mT/m and 20.34 kHz, which yielded a peak slew rate of 5112 T/m/s, a maximum spectral bandwidth of 20.34 kHz (68 ppm), and a k-space coverage of $\Delta k_{silent} = 27.1$ m^{-1}. This k-space coverage allowed for a 5.2-fold reduction in phase-encoding steps, which would result in 6.2 phase-encoding steps. Consequently, the silent EPSI acquisition featured $32 \times 7 = 224$ phase-encoding steps with an acquisition time of 3 min 44 s (Figure 1D). A comparison with the spatial encoding feasible using whole-body gradients at 20.34 kHz ($SR_{max} = 200$ T/m/s) is shown in Supporting Information Figure S1. The silent EPSI readout was sampled continuously with a sampling frequency of 488 kHz (i.e., 24 samples per oscillation period of the ultrasonic gradient). This oversampling ensured that the Nyquist criterion was satisfied in the direction of the silent gradient, as this yielded a maximum distance between k-space samples of $\Delta k_z = 3.44$ m^{-1}, which corresponded to an FOV of 289 mm.

2.3.2 | Conventional EPSI

The conventional EPSI was acquired using a maximum slew rate of 166 T/m/s and a gradient strength of 15.65 mT/m, which corresponded to a readout bandwidth of 128 kHz and a spectral bandwidth of 2279 Hz (7.6 ppm). No ramp-sampling was used, and seven averages were acquired to match the acquisition time of the silent EPSI. A single-shot EPSI acquisition without water suppression

nor phase encoding was used as a reference scan to perform EPSI phase correction.[13]

2.3.3 | Phase-encoded MRSI

The phase-encoded MRSI featured a spectral bandwidth of 18 232 Hz (61 ppm) and 32×32 phase-encoding steps, which resulted in a scan time of 17 min 4 s.

2.4 | Sound measurements

Sound measurements were performed using a condenser microphone (Behringer ECM8000) calibrated with a 94-dB noise source (Bruel & Kjaer sound level calibrator type 4231). During the measurements, the microphone was positioned within the gradient insert and receive coil, aligning it with the subject's ear location during scanning. Subsequently, the audio data underwent *MATLAB* (MathWorks, Natick, MA, USA) processing to simulate the slow response characteristics and output of a sound level meter. This entailed applying an exponential time-domain filter and A-weighting to the acquired data.

2.5 | SNR and scan efficiency

The SNR efficiency allows for a comparison of different scans independent of imaging and is given by the SNR divided by the square root of the imaging time (SNR/$\sqrt{\text{imaging-time}}$).[32] In this analysis, SNR per voxel for various acquisitions was calculated by dividing the maximum non-water peak (acetate at 1.9 ppm) by the SD of the noise-only region in the absorption mode of the spectrum, after the zeroth and first-order phase correction. To determine the scan efficiency, the SNR efficiency was scaled using the SNR efficiency obtained from phase-encoded MRSI, effectively converting it into scan efficiency when compared with both silent and conventional EPSI.

2.6 | Reconstruction

2.6.1 | Silent EPSI

The k-space trajectory from the silent EPSI readout resulted in a non-Cartesian filling of k-space. Therefore, the data were reconstructed offline in *MATLAB* (MathWorks) using a nonuniform Fourier transform (GPUNUFFT[33]) and an iterative conjugate-gradient SENSE reconstruction with Tikhonov regularization ($\lambda = 10^{-5}$).[34] Inputs to this conjugate-gradient SENSE reconstruction were the k-space trajectory and a coil

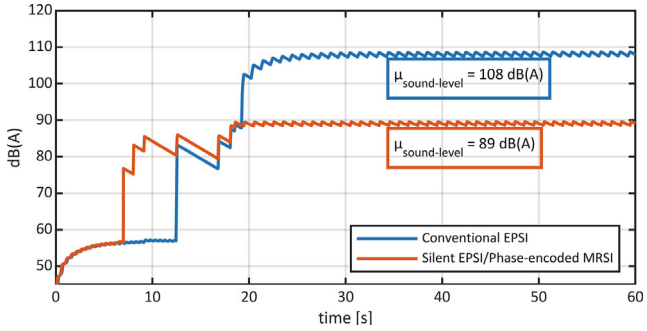

FIGURE 2 Sound level during the first 40 s of the conventional echo-planar spectroscopic imaging (EPSI), silent EPSI, and phase-encoded MRSI acquisitions. Here, the silent EPSI and phase-encoded MRSI produced identical sound levels as they featured identical audible gradient waveforms. The sound level during the silent EPSI was 19 dB lower than during the conventional EPSI, and the remaining sound originated from the VAPOR water suppression, phase-encoding gradients, and spoiling gradients. The audio clips for the different measurements can be found in the Supporting Information (Supporting Information Video S1, EPSI; Supporting Information Video S2, phase-encoded MRSI; and Supporting Information Video S3, silent EPI).

sensitivity map. Here, the k-space trajectory was based on data obtained using field camera measurements (Dynamic Field Camera; Skope, Switzerland). The variations in sample density during the readout were compensated by a density compensation function (DCF) based on the Jacobian determinant of the k-space trajectory,[35] using the following expression:

$$\mathrm{DCF} = \left| \frac{\gamma}{2\pi} G \sin(2\pi f t) \right| \tag{4}$$

An additional density compensation was applied to overlapping k-space samples from different EPSI readouts, which were assigned half the value of the DCF from Eq. (4). Coil sensitivity maps were obtained using ESPIRiT from a low-resolution gradient-echo scan acquired in 47 s.[36]

2.6.2 | Conventional EPSI and phase-encoded MRSI

The conventional EPSI and phase-encoded MRSI data were reconstructed offline in *MATLAB*. The odd and even echoes of the EPSI acquisition were aligned using gradient delays estimated from the reference scan and a phase-correction scheme similar to what is used in EPI.[13,37] The reconstruction of both the EPSI and phase-encoded MRSI data was performed using a conventional Fourier transform, after which coil combination was performed using whitened singular value decomposition based on a noise-covariance matrix obtained from acquired noise samples.[38]

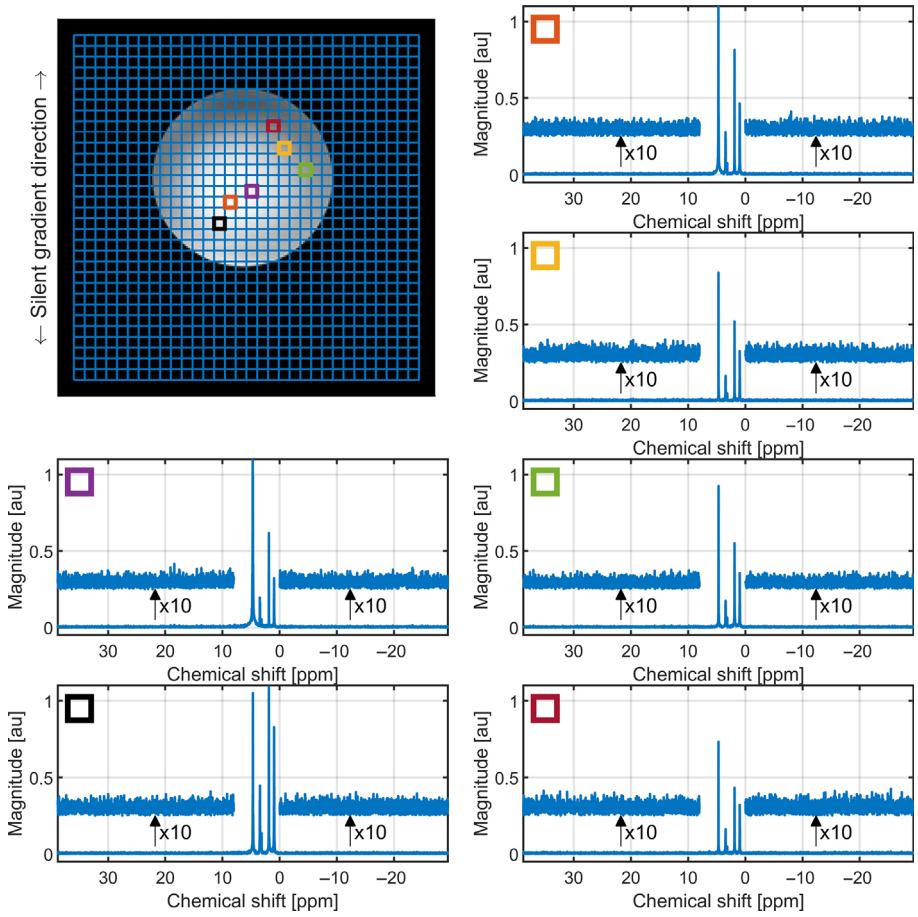

FIGURE 3 Spectra from a number of randomly selected voxels in the phantom, where the full spectral bandwidth of 20.34 kHz is shown. Here, all spectra showed the expected compounds, while no spectral aliasing was visible at the edges of the spectra.

3 | RESULTS

3.1 | Sound measurements

Figure 2 shows the sound level during the first 40 s of the conventional EPSI, silent EPSI, and phase-encoded MRSI acquisitions. Here, the silent EPSI and phase-encoded MRSI produced identical sound levels, as they featured identical audible gradient waveforms. The sound level during the silent EPSI was 19 dB lower compared with the conventional EPSI. The remaining sound was attributed to the VAPOR water suppression, phase-encoding gradients, and spoiling gradients.

3.2 | Spectroscopic imaging

Figure 3 shows a selection of voxels from the phantom for silent EPSI acquisition. Here, the full spectral bandwidth of 20.34 kHz, for ^{1}H spectroscopy, corresponded to a spectral bandwidth of 68 ppm. The four non-water peaks were detected across the phantom. In the spectral range of −30 to 0 ppm and 8 to 40 ppm, only noise and no spectral aliasing were visible in the spectra (Figure 3).

Figure 4A shows the spectral bandwidth of the silent EPSI readout compared with the phase-encoded MRSI and conventional EPSI. Here, the silent EPSI produced similar spectral bandwidth to the phase-encoded MRSI acquisition. Compared with the conventional EPSI, the silent EPSI readout produced an almost 10-fold-higher spectral bandwidth. Figure 4A also shows the spectral aliasing (red arrows) that was observed in some voxels of the conventional EPSI acquisition. Figure 4B shows the real component of the different acquisitions in the spectral range of 0 to 4 ppm. Here, all acquisitions resolved the four compounds present in the phantom.

3.3 | SNR efficiency

Figure 5 shows the SNR efficiency in each voxel for the different acquisitions. Here, the same spatial distribution of SNR was observed in all acquisitions, which correlated with the effectiveness of the water suppression. On average, the silent EPSI readout produced an SNR efficiency of 11.32, whereas the phase-encoded MRSI and conventional EPSI produced SNRs of 13.75 and 7.08, respectively. This resulted in a scan efficiency of 82.3% for the silent EPSI-readout versus 51.5% for the conventional EPSI (without ramp-sampling).

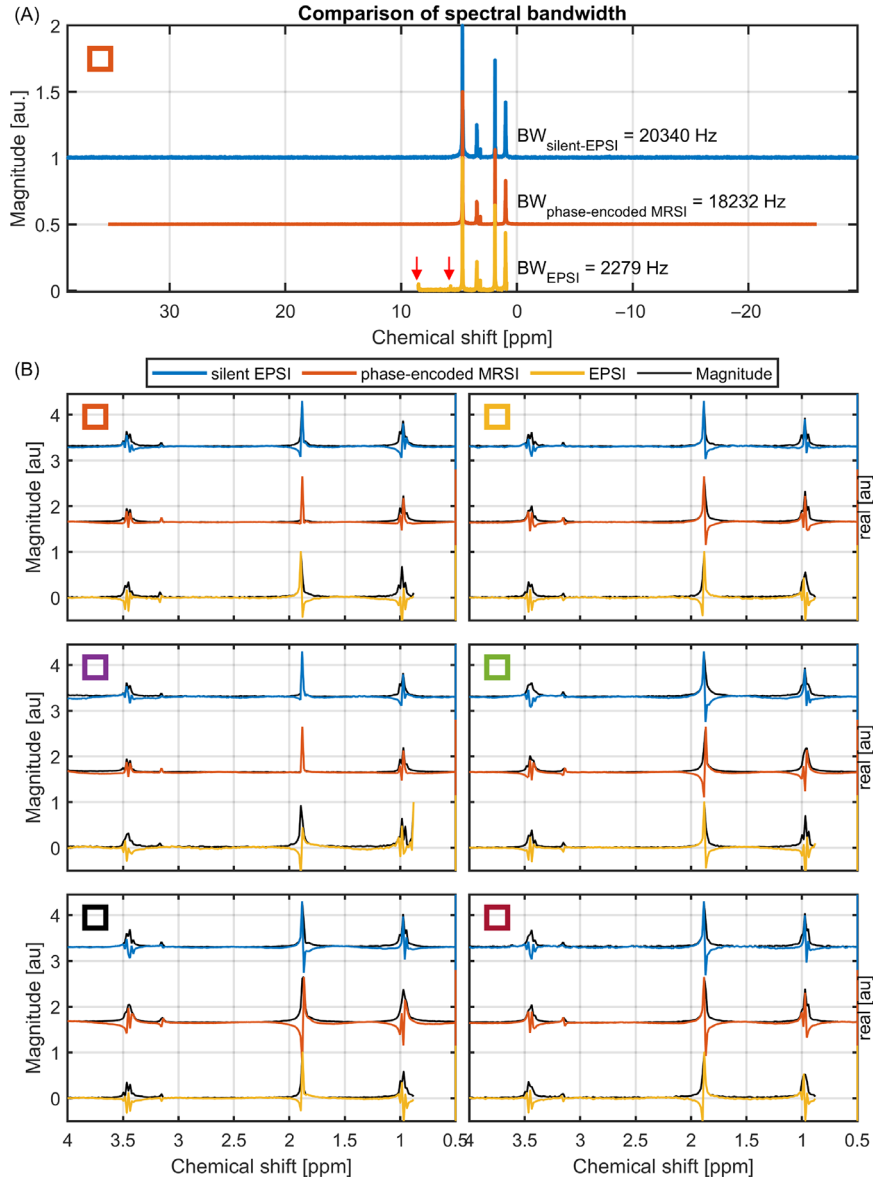

FIGURE 4 (A) Comparison of the spectral bandwidth acquired with the different acquisition methods. Note that the bandwidth (BW) for phase-encoded MRSI can still be increased arbitrarily. The red arrows indicate spectral aliasing in the conventional echo-planar spectroscopic imaging (EPSI) acquisition. (B) Phased spectra (both zeroth and first-order phasing) showcasing the spectra in the range of brain metabolites (0.5–4 ppm). Here, the same randomly selected voxels as in Figure 2 are shown.

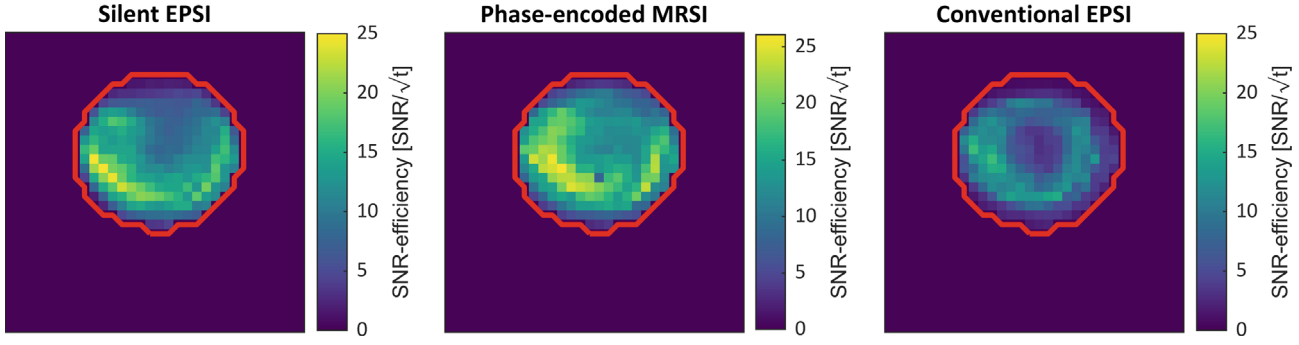

FIGURE 5 Voxel-wise SNR efficiency for the different acquisition methods. The red line indicates the area used for calculating the average SNR efficiency Note that the variation in SNR across the phantom related to spatial variations in water suppression and was similar for the different acquisitions. EPSI, echo-planar spectroscopic imaging.

4 | DISCUSSION

In this work, we have demonstrated a novel silent EPSI readout that featured a 19-dB-lower sound level and order of magnitude higher spectral bandwidth than a conventional EPSI readout with a 4.5-fold decrease in scan time compared with phase-encoded MRSI. Here, the silent EPSI readout was produced by an ultrasonic gradient insert that allowed for encoding at frequencies inaudible to the human ear. Consequently, the silent EPSI readout could benefit MRSI studies of patients who are more sensitive to acoustic noise and are likely to move during longer scans, such as pediatric patients, the elderly, or people with a psychiatric disorder.[39–42]

The ultrasonic gradient insert enabled an order of magnitude higher spectral bandwidth (~20 vs. ~2 kHz) when compared with an EPSI readout without ramp-sampling. This spectral bandwidth was independent of resolution, as the resolution in the silent EPSI depends on the number of shots acquired. The scan efficiency of the silent readout was shown to be higher than an EPSI readout without ramp sampling (82.5% vs. 51.5%) but 17.5% lower than that of phase-encoded MRSI, despite both acquisitions featuring continuous sampling. This reduction in scan efficiency is also present in other spectral-spatial encoding techniques featuring non-Cartesian readouts and originates from the nonuniform k-space sampling of the data.[16,43,44] Importantly, this also means that ramp-sampled EPSI is expected to have a higher SNR efficiency than the silent EPSI acquisition.[43]

At 7 T, the spectral bandwidth produced by the silent EPSI readout might not be necessary, as it covers a much wider range than the approximate 3-kHz spectral bandwidth needed to cover the 0–4 ppm range needed for ^{1}H brain metabolites.[45] However, this high spectral bandwidth can benefit ^{31}P-MRSI experiments, which typically need a spectral bandwidth of 5 kHz at 7 T,[20,46,47] or even for ^{13}C and ^{19}F, which chemical shifts can extend to 100 ppm. The silent EPSI readout should also benefit new ultrahigh-field MR systems (e.g., 10.4 T, 11.7 T, 14 T),[3,48] which intrinsically feature demand for higher spectral bandwidth.

4.1 | Current limitations

The gradient insert used in this work operated in the z-direction, which means the scan orientation for 2D scans was limited to sagittal or coronal. Furthermore, the scan-time reduction from the silent EPSI readout was less than with a conventional EPSI readout, which was caused by the limited spatial encoding provided by the fast-oscillating gradient field. Both these limitations could be addressed by extending the silent gradient concept to multiple axes,[49] which would allow for more flexibility in scan orientation for 2D scans and additional spatial encoding per TR for a further reduction in scan time. Alternatively, the silent EPSI readout could be combined with a conventional EPSI readout in the x-direction or y-direction, where it can compensate for a quieter, lower-amplitude EPI readout to enable fast high bandwidth and resolution MRSI with lower sound levels. Moreover, we used an audio amplifier that provides several orders of magnitude lower current than conventional gradient amplifiers can. High-bandwidth conventional amplifiers are being developed that could increase spatial encoding and yield faster silent readouts.[50]

5 | CONCLUSIONS

We have demonstrate, for the first time, a silent spectroscopic imaging readout that offers a substantial spectral bandwidth of 20.34 kHz, coupled with a 4.5-fold reduction in scan time compared with phase-encoded MRSI. The significant reduction in sound pressure from the silent readout holds potential benefits for sound-sensitive patient groups, whereas the broad spectral bandwidth opens new possibilities for ultrahigh-field MR systems.

ACKNOWLEDGMENTS

The Dutch Research Council (NWO-VIDI Wijnen-18361), European Union's Horizon 2020 Marie Sklodowska-Curie grant INSPIRE-MED (813120), and EUROSTARS Funding Project E! 11362 BEYOND.

ORCID

Edwin Versteeg https://orcid.org/0000-0003-3235-3970
Kyung Min Nam https://orcid.org/0000-0002-9185-3986
Alex A. Bhogal https://orcid.org/0000-0003-3211-1760
Jeroen C. W. Siero https://orcid.org/0000-0001-5079-2868
Jannie P. Wijnen https://orcid.org/0000-0003-2352-3667

REFERENCES

1. Hakumäki JM, Poptani H, Sandmair AM, Ylä-Herttuala S, Kauppinen RA. 1H MRS detects polyunsaturated fatty acid accumulation during gene therapy of glioma: implications for the in vivo detection of apoptosis. *Nat Med.* 1999;5:1323-1327. doi:10.1038/15279
2. Hangel G, Niess E, Lazen P, Bednarik P, Bogner W, Strasser B. Emerging methods and applications of ultra-high field MR spectroscopic imaging in the human brain. *Anal Biochem.* 2022;638:114479. doi:10.1016/j.ab.2021.114479
3. Ladd ME, Bachert P, Meyerspeer M, et al. Pros and cons of ultra-high-field MRI/MRS for human application. *Prog Nucl*

Magn Reson Spectrosc. 2018;109:1-50. doi:10.1016/j.pnmrs.2018.06.001

4. Henning A, Fuchs A, Murdoch JB, Boesiger P. Slice-selective FID acquisition, localized by outer volume suppression (FIDLOVS) for 1H-MRSI of the human brain at 7 T with minimal signal loss. *NMR Biomed.* 2009;22:683-696. doi:10.1002/nbm.1366
5. Bogner W, Gruber S, Trattnig S, Chmelik M. High-resolution mapping of human brain metabolites by free induction decay 1H MRSI at 7T. *NMR Biomed.* 2012;25:873-882. doi:10.1002/nbm.1805
6. Boer VO, Van De Lindt T, Luijten PR, Klomp DWJ. Lipid suppression for brain MRI and MRSI by means of a dedicated crusher coil. *Magn Reson Med.* 2015;73:2062-2068. doi:10.1002/mrm.25331
7. Nassirpour S, Chang P, Henning A. High and ultra-high resolution metabolite mapping of the human brain using 1H FID MRSI at 9.4T. *Neuroimage.* 2018;168:211-221. doi:10.1016/j.neuroimage.2016.12.065
8. Hangel G, Strasser B, Považan M, et al. Lipid suppression via double inversion recovery with symmetric frequency sweep for robust 2D-GRAPPA-accelerated MRSI of the brain at 7T. *NMR Biomed.* 2015;28:1413-1425. doi:10.1002/nbm.3386
9. Kirchner T, Fillmer A, Tsao J, Pruessmann KP, Henning A. Reduction of voxel bleeding in highly accelerated parallel 1H MRSI by direct control of the spatial response function. *Magn Reson Med.* 2015;73:469-480. doi:10.1002/mrm.25185
10. Nassirpour S, Chang P, Avdievitch N, Henning A. Compressed sensing for high-resolution nonlipid suppressed 1H FID MRSI of the human brain at 9.4T. *Magn Reson Med.* 2018;80:2311-2325. doi:10.1002/mrm.27225
11. Hingerl L, Bogner W, Moser P, et al. Density-weighted concentric circle trajectories for high resolution brain magnetic resonance spectroscopic imaging at 7T. *Magn Reson Med.* 2018;79:2874-2885. doi:10.1002/mrm.26987
12. Hangel G, Cadrien C, Lazen P, et al. High-resolution metabolic imaging of high-grade gliomas using 7T-CRT-FID-MRSI. *NeuroImage Clin.* 2020;28:102433. doi:10.1016/j.nicl.2020.102433
13. Coello E, Noeske R, Burns BL, et al. High-resolution echo-planar spectroscopic imaging at ultra-high field. *NMR Biomed.* 2018;31:e3950. doi:10.1002/nbm.3950
14. Nam KM, Hendriks AD, Boer VO, Klomp DWJ, Wijnen JP, Bhogal AA. Proton metabolic mapping of the brain at 7 T using a two-dimensional free induction decay-echo-planar spectroscopic imaging readout with lipid suppression. *NMR Biomed.* 2022;35:e4771. doi:10.1002/nbm.4771
15. Nam KM, Gursan A, Bhogal AA, et al. Deuterium echo-planar spectroscopic imaging (EPSI) in the human liver in vivo at 7 T. *Magn Reson Med.* 2023;90:863-874. doi:10.1002/mrm.29696
16. Bogner W, Otazo R, Henning A. Accelerated MR spectroscopic imaging—a review of current and emerging techniques. *NMR Biomed.* 2021;34:e4314. doi:10.1002/nbm.4314
17. Posse S, Tedeschi G, Risinger R, Ogg R, Le Bihan D. High speed 1H spectroscopic imaging in human brain by echo planar spatial-spectral encoding. *Magn Reson Med*. 1995;33:34-40. doi:10.1002/mrm.1910330106
18. Posse S, DeCarli C, Le Bihan D. Three-dimensional echo-planar MR spectroscopic imaging at short echo times in the human brain. *Radiology*. 1994;192:733-738. doi:10.1148/radiology.192.3.8058941
19. Matsui S, Sekihara K, Kohno H. Spatially resolved nmr spectroscopy using phase-modulated spin-echo trains. *J Magn Reson.* 1986;67:476-490. doi:10.1016/0022-2364(86)90385-9
20. Korzowski A, Bachert P. High-resolution 31P echo-planar spectroscopic imaging in vivo at 7T. *Magn Reson Med.* 2018;79:1251-1259. doi:10.1002/mrm.26785
21. An Z, Tiwari V, Ganji SK, et al. Echo-planar spectroscopic imaging with dual-readout alternated gradients (DRAG-EPSI) at 7 T: application for 2-hydroxyglutarate imaging in glioma patients. *Magn Reson Med.* 2018;79:1851-1861. doi:10.1002/mrm.26884
22. An Z, Tiwari V, Baxter J, et al. 3D high-resolution imaging of 2-hydroxyglutarate in glioma patients using DRAG-EPSI at 3T in vivo. *Magn Reson Med.* 2019;81:795-802. doi:10.1002/mrm.27482
23. Labadie C, Hetzer S, Schulz J, Mildner T, Aubert-Frécon M, Möller HE. Center-out echo-planar spectroscopic imaging with correction of gradient-echo phase and time shifts. *Magn Reson Med.* 2013;70:16-24. doi:10.1002/mrm.24428
24. Adalsteinsson E, Irarrazabal P, Topp S, Meyer C, Macovski A, Spielman DM. Volumetric spectroscopic imaging with spiral-based k-space trajectories. *Magn Reson Med.* 1998;39:889-898. doi:10.1002/mrm.1910390606
25. Furuyama JK, Wilson NE, Thomas MA. Spectroscopic imaging using concentrically circular echo-planar trajectories in vivo. *Magn Reson Med.* 2012;67:1515-1522. doi:10.1002/MRM.23184
26. Schirda CV, Tanase C, Boada FE. Rosette spectroscopic imaging: optimal parameters for alias-free, high sensitivity spectroscopic imaging. *J Magn Reson Imaging.* 2009;29:1375-1385. doi:10.1002/jmri.21760
27. Fletcher H, Munson WA. Loudness, its definition, measurement and calculation. *Bell Syst Tech J.* 1933;12:377-430. doi:10.1002/j.1538-7305.1933.tb00403.x
28. McJury MJ. Acoustic noise and magnetic resonance imaging: a narrative/descriptive review. *J Magn Reson Imaging.* 2022;55:337-346. doi:10.1002/jmri.27525
29. Versteeg E, Klomp DWJ, Siero JCW. A silent gradient axis for soundless spatial encoding to enable fast and quiet brain imaging. *Magn Reson Med.* 2022;87:1062-1073. doi:10.1002/mrm.29010
30. Versteeg E, Klomp DWJ, Siero JCW. Accelerating brain imaging using a silent spatial encoding axis. *Magn Reson Med.* 2022;88:1785-1793. doi:10.1002/mrm.29350
31. Versteeg E, van der Velden TA, van Leeuwen CC, et al. A plug-and-play, lightweight, single-axis gradient insert design for increasing spatiotemporal resolution in echo planar imaging-based brain imaging. *NMR Biomed.* 2021;34:e4499. doi:10.1002/nbm.4499
32. Parker DL, Gullberg GT. Signal-to-noise efficiency in magnetic resonance imaging. *Med Phys*. 1990;17:250-257. doi:10.1118/1.596503
33. Knoll F, Schwarzl A, Diwoky Z, Sodickson DK. gpuNUFFT—an open-source GPU library for 3D gridding with direct Matlab and python Interface. *Proceedings of the 22nd Annual Meeting of ISMRM, Milano*; ISMRM; 2014:4297.
34. Pruessmann KP, Weiger M, Börnert P, Boesiger P. Advances in sensitivity encoding with arbitrary *k*-space trajectories. *Magn Reson Med.* 2001;46:638-651. doi:10.1002/mrm.1241
35. Hoge RD, Kwan RKS, Pike GB. Density compensation functions for spiral MRI. *Magn Reson Med*. 1997;38:117-128. doi:10.1002/mrm.1910380117

36. Uecker M, Lai P, Murphy MJ, et al. ESPIRiT—an eigenvalue approach to autocalibrating parallel MRI: where SENSE meets GRAPPA. *Magn Reson Med.* 2014;71:990-1001. doi:10.1002/mrm.24751
37. Bruder H, Fischer H, Reinfelder H-E, Schmitt F. Image reconstruction for echo planar imaging with nonequidistant k-space sampling. *Magn Reson Med.* 1992;23:311-323. doi:10.1002/mrm.1910230211
38. Rodgers CT, Robson MD. Receive array magnetic resonance spectroscopy: whitened singular value decomposition (WSVD) gives optimal bayesian solution. *Magn Reson Med*. 2010;63:881-891. doi:10.1002/mrm.22230
39. Moelker A, Maas RAJJ, Pattynama PMT. Verbal communication in MR environments: effect of MR system acoustic noise on speech understanding. *Radiology.* 2004;232:107-113. doi:10.1148/radiol.2321030955
40. McJury M, Shellock FG. Auditory noise associated with MR procedures: a review. *J Magn Reson Imaging.* 2000;12:37-45. doi:10.1002/1522-2586(200007)12:1<37::AID-JMRI5>3.0.CO;2-I
41. Edwards AD, Arthurs OJ. Paediatric MRI under sedation: is it necessary? What is the evidence for the alternatives? *Pediatr Radiol.* 2011;41:1353-1364. doi:10.1007/s00247-011-2147-7
42. Shellock FG. *Magnetic Resonance: Bioeffects, Safety, and Patient Management*. Raven; 1994:101-121.
43. Jiang W, Lustig M, Larson PEZ. Concentric rings K-space trajectory for hyperpolarized 13C MR spectroscopic imaging. *Magn Reson Med.* 2016;75:19-31. doi:10.1002/mrm.25577
44. Tsai CM, Nishimura DG. Reduced aliasing artifacts using variable-density k-space sampling trajectories. *Magn Reson Med.* 2000;43:452-458. doi:10.1002/(SICI)1522-2594(200003)43:3<452::AID-MRM18>3.0.CO;2-B
45. Tkáč I, Öz G, Adriany G, Uğurbil K, Gruetter R. In vivo 1H NMR spectroscopy of the human brain at high magnetic fields: metabolite quantification at 4T vs. 7T. *Magn Reson Med.* 2009;62:868-879. doi:10.1002/mrm.22086
46. Qiao H, Zhang X, Zhu XH, Du F, Chen W. In vivo 31P MRS of human brain at high/ultrahigh fields: a quantitative comparison of NMR detection sensitivity and spectral resolution between 4 T and 7 T. *Magn Reson Imaging.* 2006;24:1281-1286. doi:10.1016/j.mri.2006.08.002
47. Korzowski A, Weinfurtner N, Mueller S, et al. Volumetric mapping of intra- and extracellular pH in the human brain using 31P MRSI at 7T. *Magn Reson Med.* 2020;84:1707-1723. doi:10.1002/MRM.28255
48. Budinger TF, Bird MD. MRI and MRS of the human brain at magnetic fields of 14T to 20T: technical feasibility, safety, and neuroscience horizons. *Neuroimage.* 2018;168:509-531. doi:10.1016/j.neuroimage.2017.01.067
49. Versteeg E, van der Velden TA, Klomp DW, Hendrikse J, Siero JCW. Dual axis gradient insert for supersonic MRI. *Proceedings of the 28th Annual Meeting of ISMRM*; ISMRM; 2020:617.
50. van Ieperen A, Tax C, Klomp DW, et al. Short-TE diffusion-MRI by combining strong gradients with ultrasonic readout. *Proceedings of the 30th Annual Meeting of ISMRM*; ISMRM; 2022:1367.

SUPPORTING INFORMATION

Additional supporting information may be found in the online version of the article at the publisher's website.

Figure S1. Comparison of the amount of encoding steps needed for different gradient frequencies when using a conventional whole-body gradient with a slew rate limit of 200 T/m/s. Note that the ultrasonic gradient can provide more than 20 times more spatial encoding at 20.34 kHz.

Video S1. Sound measured from the echo-planar spectroscopic imaging (EPSI) sequence used in this work.

Video S2. Sound measured from the phase-encoded MRSI sequence used in this work.

Video S3. Sound measured from the silent echo-planar spectroscopic imaging (EPSI) sequence used in this work.

How to cite this article: Versteeg E, Nam KM, Klomp DWJ, Bhogal AA, Siero JCW, Wijnen JP. A silent echo-planar spectroscopic imaging readout with high spectral bandwidth MRSI using an ultrasonic gradient axis. *Magn Reson Med*. 2024;91:2247-2256. doi: 10.1002/mrm.30008